



# Erosion analysis and experimental research of gas-liquid-solid soft abrasive flow polishing based on cavitation effects

Man Ge<sup>1,2</sup> · Shiming Ji<sup>1,2</sup> · Dapeng Tan<sup>1,2,3</sup> · Huiqiang Cao<sup>1,2</sup>

Received: 30 May 2020 / Accepted: 1 February 2021 / Published online: 26 April 2021  
© The Author(s), under exclusive licence to Springer-Verlag London Ltd., part of Springer Nature 2021

## Abstract

Traditional soft abrasive flow (SAF) polishing is limited by its low material removal rate and its applicability to large workpieces. To address this issue, an innovative technique of a cavitation-based gas-liquid-solid abrasive flow polishing (CGLSP) process is proposed. The energy generated from cavitation effects is employed to increase the kinetic energy of abrasive particles in the fluid flow and the random movement of abrasive particles near the surface. The CGLSP mechanism is first introduced, and then, the cavitation erosion characteristics and material removal mechanism of brittle-plastic materials during polishing are investigated using a coupling computational fluid dynamics model. The simulated results show that erosion of the workpiece surface mainly occurs in the spiral area of the polishing tool. Furthermore, the erosion rate and erosion depth increase with increasing cavitation intensity. Subsequently, polishing experiments are conducted to verify the validity of the CGLSP method. The polishing results are verified by scanning electron microscopy (SEM) images of the polished surface. After polishing with the CGLSP method, most of the surface irregularities, such as microcracks and massive structures, are removed. The experimental results demonstrate that controlled polishing with cavitation erosion and abrasion can achieve a much higher quality surface on a large workpiece.

**Keywords** Cavitation erosion · Prediction method · Brittle-plastic materials, · Material removal mechanism

## 1 Introduction

With the development of modern science and technology, more stringent requirements have been put forward for electronic systems [1]. As raw materials of the semiconductor industry, brittle-plastic materials such as monocrystalline silicon and K9 glass must be processed in a plastic way on their surfaces, which is the key to ensure no scratches, pockmarks, or subsurface damage [2]. Compared with most tool-contact

processing methods that cause surface and subsurface defects, the good adaptability and micromachining properties of soft abrasive flow (SAF) seem to provide a good solution for processing brittle-plastic materials, and indeed, this method has been widely used for the deburring, processing mark removal, and precision polishing of complex structured surfaces with small amounts of material removed from the target [3, 4].

Due to the beneficial effects of SAF processing methods, considerable research has been conducted. In 2010, Ji et al. [5–7] established the two-phase dynamic model and simulation of SAF based on a discrete phase model (DPM), and their simulation results showed that the abrasive flow process is mainly manifested by the effects of particle pressure and near-wall particle velocity. In 2011, Sankar et al. [8] performed an experimental study on aluminum alloy and its metal matrix composites using a rotating abrasive flow finishing process and derived the relationships among related parameters for roughness and material removal. In 2012, Li et al. [9] studied the motion law of the SAF method on the surface of a small-scale mold structure according to the experimental principle of Nikuradse and obtained a suitable friction coefficient formula. Their experimental results show that the SAF method

✉ Dapeng Tan  
tandapeng@zjut.edu.cn

<sup>1</sup> College of Mechanical Engineering, Zhejiang University of Technology, Hangzhou 310023, China

<sup>2</sup> Key Laboratory of Specially Purpose Equipment and Advanced Processing Technology, Ministry of Education and Zhejiang Province, Zhejiang University of Technology, Hangzhou 310023, China

<sup>3</sup> Collaborative Innovation Center of High-End Laser Manufacturing Equipment (National “2011 Plan”), Zhejiang University of Technology, Hangzhou 310023, China

can achieve a workpiece surface roughness as low as 62 nm. In 2016, Tan et al. [10] proposed a new type of double-inlet SAF finishing method based on the fluid collision theory for a current SAF finishing method with surface quality problems caused by uneven flow. Their processing experiments showed that the proposed SAF finishing method can achieve a roughness in the parallel flow direction of less than 50 nm and can improve the finishing uniformity and efficiency.

In the SAF process, particle velocity and fluid medium turbulence characteristics may affect processing efficiency and quality. Related studies have shown that the collapse of bubbles will increase the degree of turbulence in a fluid field, and research has been conducted regarding the enhancement of turbulent flows by bubble collapse [11–13]. Zhang et al. [14] proposed a gas compensation-based abrasive flow (GCAF) treatment method for complex titanium alloy surfaces, and their results proved that the proposed method could obtain better processing efficiency and uniformity. Ge et al. [15] proposed a gas-liquid-solid three-phase abrasive flow processing method (GLSP) based on bubble collapse to solve the problem of low efficiency of the SAF method. A large number of experiments proved that the GLSP method could increase the processing efficiency by 50% compared with the SAF method, and the average surface roughness could reach 2.84 nm. Compared with the limited collapsing energy of ordinary micro-/nanobubbles, a high-density energy of  $1\sim 1018\text{ kW/m}^3$  could be released when the cavitation bubbles collapse, accompanied by high temperature and high pressure [16]. The collapse of the cavitation cloud in the fluid field produces a strong shock wave and high-energy microjet near the microbubbles, which is expected to improve the degree of turbulence and the randomness of abrasive particle movement in the fluid field. In addition, the efficiency of fluid polishing was improved, which may be a promising method of fluid polishing [17–19].

The processing mechanism of an abrasive flow is the result of the repeated impact of abrasive particles driven by the fluid medium in the fluid field on the surface of the workpiece, which is similar to erosion wear in the fields of mining, metallurgy, and pipeline transportation. One approach to investigate cavitation erosion is to employ computational fluid dynamics (CFD) methods [20–22]. This approach-oriented erosion wear can be divided into two categories: an Eulerian-Lagrangian method (E-L) [23] and a Eulerian-Eulerian method (E-E) [24]. In the hypothesis of the E-L method, the particles are considered discrete phases with a low volume fraction, and only the effect of continuous relative discrete phases is considered. Nguyen et al. [25] used the E-L method to study how particle size affects erosion characteristics, and their experimental results showed that there is a transition in the erosion profile from a W-shape to a U-shape with increasing sand particle size. Duarte et al. [26] adopted an accurate computational fluid dynamics model based on the Euler-Lagrangian

method to evaluate erosion depth for a new type of pipe wall design. Their simulations showed that a reduction in the erosion peak up to 33% could be achieved in a pipeline equipped with a twisted pipe wall in comparison to the baseline configuration. With respect to the E-E method, different phases are treated as continuous media running through each other. Messa et al. [27] improved the E-E method for the complex physical phenomena of slurry erosion and obtained high accuracy in several abrasive jet impingement experiments. Zahedi et al. [28] used the fluid volume method (VOF) and E-L method to simulate air-water flows with high gas velocities and low liquid rates. The same flow rate was obtained by the two simulation methods and was consistent with the experimental results. In view of the soft abrasive flow in this paper, the particle is mainly driven by the fluid medium to micromachine the target, and the particle content is low. Therefore, the E-L method is used to describe the entire erosion process more accurately.

In this paper, gas-liquid-solid three-phase flow under cavitating conditions along with abrasive particles is explored for use as a possible surface polishing technique. Considering that cavitation bubbles are added to the abrasive flow, the fluid flow characteristics and surface erosion behavior are demonstrated using a coupling computational fluid dynamics model. Extensive polishing experiments are conducted to verify the accuracy of the prediction results of the material removal distribution in a polishing process. Furthermore, improvements in the workpiece surface of brittle-plastic materials are discussed using qualitative results obtained from scanning electron microscope (SEM) images.

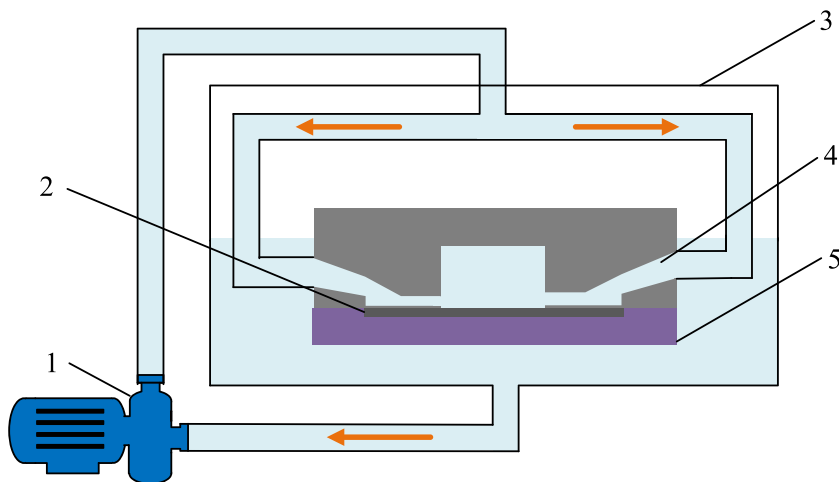
This paper is organized as follows. In Section 2, the working principle of the CGLSP method is introduced, and the polishing tool is designed. In Section 3, the three-phase fluid mechanics model of the CGLSP method is set up based on a hybrid Euler-Lagrangian framework, cavitation model, and erosion model. In Section 4, numerical simulations of the surface erosion characteristics in gas-liquid-solid abrasive flow and a comparison analysis and discussion are performed. In Section 5, a CGLSP polishing experimental platform is set up, and experiments are conducted. In Section 6, the conclusions are presented.

## 2 Polishing theory

### 2.1 Design of the CGLSP polishing tool

Based on our previous work [29–31], a polishing tool constructed using a multi-inlet constrained fluid channel is designed. By constructing the confined fluid channel on the workpiece surface, soft abrasive flow is employed instead of a machining tool to achieve polishing of the workpiece surface to avoid surface and subsurface damage. As shown in Fig. 1,

**Fig. 1** Abridged general view of CGLSP polishing tool. 1, abrasive flow pump; 2, workpiece; 3, tank; 4, CGLSP polishing tool nozzle; 5, vacuum plate



the workpiece is fixed on a vacuum suction plate, and the polishing tool is mounted approximately 1 mm from the target surface. Then, the workpiece and the polishing tool are placed into a processing tank filled with gas-liquid mixed fluid medium with abrasive grains. The soft abrasive flow is injected into the fluid channel by a high-pressure pump through the four inlets.

The geometric structure and working principle of the polishing tool are shown in Fig. 2. The polishing tool consists of a cavitation-constrained fluid channel and an observation

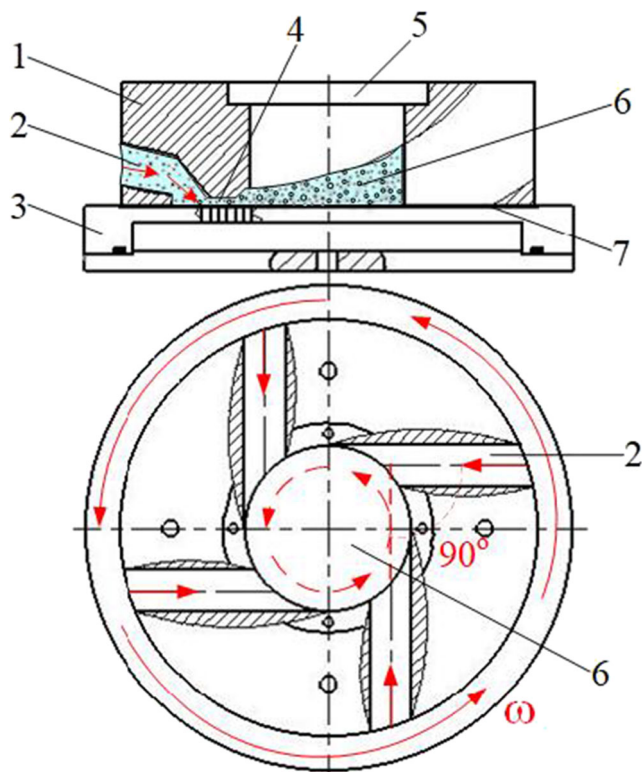


**Fig. 2** Structural diagram of CGLSP polishing tool. 1, polishing tool; 2, inlet; 3, vacuum plate; 4, flow channel; 5, observation window; 6, vortex area; 7, outlet

window. When the four-grit abrasive flow gathers in a nonconstrained space and forms a high-speed vortex [32], it enters the confined space in a high-speed swirling manner that is formed by the workpiece and polishing tool. Due to the drastic reduction in the volume of the fluid channel, the probability of collisions between the abrasive particles and the polished surface is increased. When abrasive flow passes through the constrained fluid channel, cavitation bubbles form and collapse, which will release a large amount of energy. The energy generated by cavitation bubble collapse can increase the impact kinetic energy of the abrasive particles and enhance the turbulence intensity of the local fluid flow, thereby further improving the processing efficiency and quality.

### 2.2 Cavitation effects and erosion verification

Due to the small size of the microbubbles and the short bubble collapse time, it is difficult to observe them without any equipment. The method shown in Fig. 3 offers us the possibility of demonstrating the existence of cavitation effects. Using a similar principle, a single runner was designed. Pure water was pumped through the pump in the direction shown in Fig. 3a, and a high-speed camera was used to photograph the fluid channel. The results obtained are shown in Fig. 3b–d. From 0 to 2.162 s, when high-pressure fluid passes through the contraction section to the expansion channel, cavitation bubbles are generated in the fluid channel. The pressure at the inlet of the fluid channel is 0.6 MPa. From this observation, we can determine that the cavitation effects in the fluid channel will continue to increase as the pressure continues to increase.

To better analyze the principle and modeling of the CGLSP method in the following text, preliminary polishing experiments are carried out. The results of observing the silicon wafer surface with a microscope are shown in Fig. 4. The initial surface of the silicon wafer is very rough and shows a large number of pit shapes. After 2 h of processing, the surface

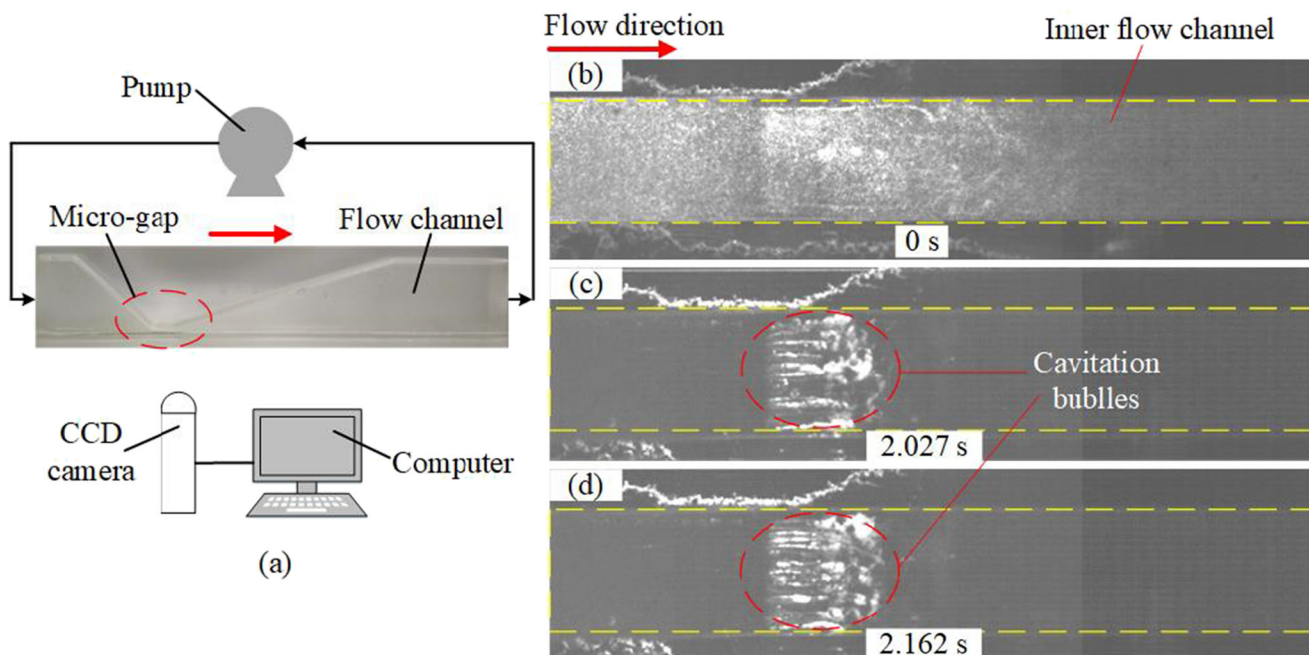


Fig. 3 Observation results of the fluid channel

irregularities of the workpiece were partially removed. It can be seen that a large amount of erosion traces appears on the silicon wafer surface in Fig. 4b and c. From the above experiments, it can be presumed that the material removed by the CGLSP process is erosion wear.

### 2.3 Analysis of near-wall microcutting characteristics

Figure 5a shows the processing of abrasive flow in the near-wall area under the effect of cavitation. Relevant studies have shown that delamination occurs at the rough surface peak of the workpiece during abrasive flow processing [33–35]. The strong swirling flow formed by the multi-inlet injection abrasive flow and the low viscosity characteristics of the fluid will form a turbulent flow area on the polished surface. The role of the turbulent vortex is to carry abrasive particles on the polished surface to achieve microcutting when there are no

bubbles in the fluid field [36, 37]. However, the roughness of the workpiece surface is still in the laminar state below the peak, which will affect the smoothness of the processing. When cavitation bubbles are injected into the fluid field, the microjets and energy generated by bubble collapse can increase the impact kinetic energy of the abrasive particles. In addition, the turbulent energy induced at the interface of the bubbles can enhance the degree of turbulence in the fluid field, which not only improves the processing efficiency but also ensures polished surface smoothness.

Figure 5a and b show that a single abrasive particle of mass  $m_p$  impacts the polished surface at a certain velocity  $v_p$  and angle  $\alpha$ . When the impact kinetic energy of the abrasive particles meets the plastic shear removal of materials, the method of material removal is plowing and microcutting without radial cracks or lateral cracks. With the continuous impact of abrasive particles on the workpiece surface, the materials in

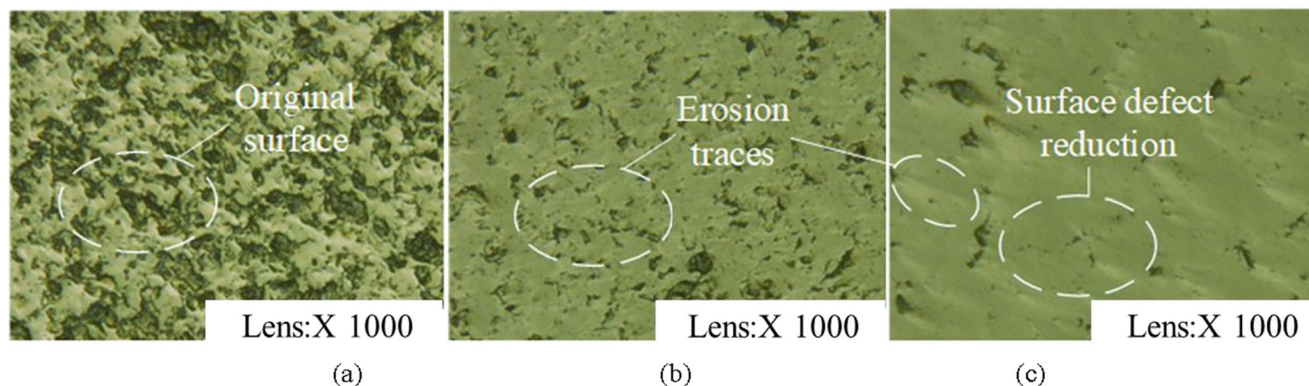
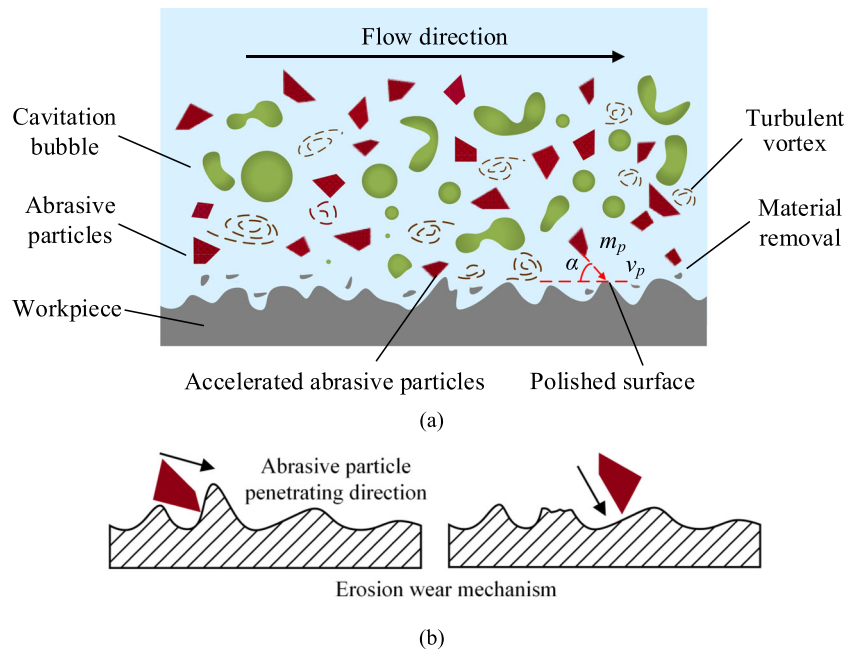


Fig. 4 Material removal principle of CGLSP process. a  $T = 0$  h. b  $T = 1$  h. c  $T = 2$  h

**Fig. 5** Processing mechanism of CGLSP process. **a** Cavitation-assisted mechanism. **b** Material removal mechanism



the indentation area will accumulate and eventually form debris. Furthermore, the abrasive particles are subjected to a variety of forces in the bubble collapse shock environment, which makes the abrasive particles appear disordered in the direction of microscopic motion, resulting in material removal as a result of comprehensive erosion of the abrasive particles at various angles [6, 38]. Hence, the surface of the workpiece can be polished without scratching in a single direction. The cavitation erosion of the polished surface removes the materials at the protrusions of the workpiece surface, which forms a smooth surface.

### 3 Numerical modeling

As indicated in Section 2, the flowing state is a gas-liquid-solid abrasive flow in a limited physical space, which involves the following four mathematical models: a fluid control model, a particle motion model, a cavitation model, and an erosion model. The numerical simulation of the soft abrasive flow based on cavitation effects is achieved using the fluid dynamics software Fluent.

#### 3.1 The Eulerian-Lagrangian model

The Euler multiphase flow model is widely used in fluid analysis because it can better describe the interactions among different phases. The mixture of the liquid phase and vapor phase in the Euler model can be considered a continuous medium, in which the continuity equation of the mixed phase can be given as:

$$\frac{\partial}{\partial t}(\rho) + \nabla \cdot (\rho \mathbf{u}) = 0 \tag{1}$$

where the density of the mixed phase  $\rho$  and vapor phase volume fraction are defined as follows:  $\rho = \rho_v \alpha_v + \rho_l (1 - \alpha_v)$  and  $\alpha_l = 1 - \alpha_v$ .  $\mathbf{u}$  is the fluid velocity, and  $\rho_v$ ,  $\rho_l$ , and  $\alpha_v$  represent the vapor phase density, liquid phase density, and vapor phase volume fraction. The momentum conservation equation is as follows when the relative slip velocity and volume force between the bubble and liquid phase are ignored:

$$\frac{\partial}{\partial t}(\rho \mathbf{u}) + \nabla \cdot (\rho \mathbf{u} \mathbf{u}) = -\nabla P + \nabla \cdot [\mu(\nabla \mathbf{u} + \nabla \mathbf{u}^T)] - \mathbf{F} \tag{2}$$

Here,  $t$  denotes time,  $P$  refers to the pressure, and  $\mu$  is the dynamic viscosity. The value of  $\mathbf{F}$  is 0 when only calculating the continuous phase. In the coupled calculation of the gas-liquid-solid three-phase medium described in this paper,  $\mathbf{F}$  only depends on the force of continuous relative discrete particles.

According to the two-phase flow theory, the motion of the abrasive particles is traced in the Lagrange framework [39]. The motion of abrasive particles can be expressed in a Cartesian coordinate system as follows:

$$\frac{d\mathbf{u}_p}{dt} = F_d(\mathbf{u} - \mathbf{u}_p) + \frac{\mathbf{g}(\rho_p - \rho)}{\rho_p} + F_{\text{other}} \tag{3}$$

where  $d/dt$  is the material derivative of the Lagrangian particle moving with velocity  $\mathbf{u}_p$ ,  $F_d$  describes forcing due to the drag, and  $\mathbf{g}$  is the gravitational acceleration. In these expressions,  $F_{\text{other}}$  is all the force acting on particles in the fluid field. These

other forces including the pressure gradient, Basset force, Saffman’s lift force, Magnus’s lift force, thermophoresis force, and buoyancy of the particles are often much smaller than the drag force. In this paper, drag forces and the gravity of particles are the dominant forces, while other forces with little effect are ignored. The drag force can be calculated by the drag force model proposed by Di Felice [39].

### 3.2 Cavitation model

The Rayleigh-Plesset equation [40] is as follows when the relative slip velocity and volume force between the bubble and liquid phase are ignored:

$$R_b \frac{d^2 R_b}{dt^2} + \frac{3}{2} \left( \frac{dR_b}{dt} \right)^2 = \frac{P_b - P_\infty}{\rho_l} - \frac{2\sigma}{\rho_l R_b} - \frac{4\mu_l}{\rho_l R_b} \frac{dR_b}{dt} \quad (4)$$

where  $\sigma$  is the surface tension between the liquid and vapor and  $P_b$  and  $P_\infty$  are the pressure in the liquid at the bubble boundary and local pressure of the fluid, respectively.  $R_b$  represents the bubble radius, and  $\mu_l$  is the dynamic viscosity.

Sauer and Schnerr defined the evaporation and condensation phases as Eqs. (5) and (6) [41]:

$$R_e = \frac{\rho_v \rho_l}{\rho_m} \alpha_v (1 - \alpha_v) \frac{3}{R_b} \sqrt{\frac{2(P_v - P)}{3\rho_l}}, \text{ when } P_v \geq P \quad (5)$$

$$R_c = \frac{\rho_v \rho_l}{\rho_m} \alpha_v (1 - \alpha_v) \frac{3}{R_b} \sqrt{\frac{2(P - P_v)}{3\rho_l}}, \text{ when } P_v \leq P \quad (6)$$

where  $P_b$  are the internal pressure of vacuoles.  $P$  and  $P_v$  are the pressure and the saturated pressure at the local temperature, respectively.

The relationship between the vapor phase volume fraction ( $\alpha_v$ ) and the number of bubbles ( $n_b$ ) in a unit liquid volume can be expressed as:

$$\alpha_v = \frac{n_b \frac{3}{4} \pi R_b^3}{1 + n_b \frac{3}{4} \pi R_b^3} \quad (7)$$

The relation of the radius of vacuoles ( $R_b$ ) can be given as:

$$R_b = \left( \frac{\alpha_v}{1 - \alpha_v} \frac{3}{4\pi n_b} \right)^{1/3} \quad (8)$$

In summary, the mutual transformation of the gas phase and liquid phase in the fluid field can be represented by the following equation:

$$\frac{\partial}{\partial t} (\alpha_v \rho_v) + \nabla \cdot (\alpha_v \rho_v \mathbf{u}) = R_e - R_c \quad (9)$$

In the Schneer-Sauer cavitation model, the bubble number density determines the vapor volume fraction, so the only empirically determined coefficient of the entire transport equation is  $n_b$ , which is defined as  $10^{13}$  [42].

### 3.3 Erosion model

When the abrasive particle bounces off the boundary after hitting the surface, the loss of energy causes the particles to rebound faster than the impact velocity. The momentum variation is determined by the collision recovery coefficient, which is decomposed into the normal recovery coefficient and tangential recovery coefficient according to the rebound velocity. The recovery coefficient formula obtained with Forder [43] is given as:

$$e_n = \frac{v_r^n}{v_m^n} = 0.988 - 0.78(\theta) + 0.19(\theta)^2 - 0.024(\theta\alpha)^3 + 0.027(\theta)^4 \quad (10)$$

$$e_t = \frac{v_r^t}{v_m^t} = 1 - 0.78(\theta) + 0.84(\theta)^2 - 0.21(\theta)^3 + 0.028(\theta)^4 - 0.022(\theta)^5 \quad (11)$$

In this paper, the Oka erosion model is adopted to predict the erosion behavior characteristics [44, 45]. Erosion damage at arbitrary angles  $E(\theta)$  can be expressed in Eq. (12).  $E(\theta)$  and  $E_{90}$  denote a unit of material volume removed per mass of particles.

$$E(\theta) = g(\theta)E_{90} \quad (12)$$

Here,  $\theta$  is the impact angle. The value of  $E_{90}$  can be calculated by Eq. (13).  $g(\theta)$  denotes the impact angle dependence of the normalized erosion by the two trigonometric functions and by the initial material hardness number  $Hv$  in units of gigapascal, as shown in Eq. (14).

$$E_{90} = K(Hv)^{k_1} \left( \frac{V_p}{V'} \right)^{k_2} \left( \frac{D_p}{D'} \right)^{k_3} \quad (13)$$

$$g(\theta) = (\sin\theta)^{n_1} (1 + Hv(1 - \sin\theta))^{n_2} \quad (14)$$

$$n_1 = s_1(Hv)^{q_1}, n_2 = s_2(Hv)^{q_2} \quad (15)$$

Here,  $n_1$  and  $n_2$  are exponents determined by the material hardness and other impact conditions, as shown in Eq. (15).  $s_1$ ,  $s_2$ ,  $q_1$ , and  $q_2$  are the fitting constants for the particle material.  $K$  denotes a particle property factor that has no correlation among different types of particles and other factors;  $k_1$ ,  $k_2$ , and  $k_3$  are exponential factors, especially  $k_2$ , which take individual values based on the type of particle. For SiC abrasive particles,  $k_2$  can be presented as [44]:

$$k_2 = 3.0(Hv)^{0.085} \quad (16)$$

In this study, the values of the coefficients mentioned above and exponents are listed in Table 1. The simulation is conducted on TC4 titanium alloy and monocrystalline silicon, and their material properties are summarized in Table 2. The erosion model is given using a user-defined function (UDF) in the Fluent software package.

### 4 Numerical simulation and result analysis

Based on the continuous medium hypothesis, an interphase coupling solution method for the cavitation erosion phenomenon is proposed, and the procedures are shown in Fig. 6. First, the mutual transformation of the gas phase and liquid phase in the fluid field can be solved, and the vapor volume fraction and vapor phase density are imported into the continuity equation. Then, the mixed medium of the liquid phase and vapor phase is discretized with fluid grid cells, and the governing equations are solved by the Euler method. If a stable solution is obtained, the relative velocities of particles and fluids are calculated, so the interaction force will be obtained. Subsequently, the motion equations of every particle are calculated by the DEM method, and the particle trajectory and kinetic characteristics of the particles are updated. At the same time, the recovery coefficient formula obtained with Forder can be obtained. Finally, the workpiece material properties and kinematic parameters are input into the erosion framework, the erosion behaviors are updated, and the material removal characteristics are obtained. After one CFD time step, the dynamic features of particles are input back into the fluid grid cells, the vapor volume fraction and vapor phase density are updated, and then, the numerical solver begins a new round of iterative calculations to constantly update the erosion characteristics.

#### 4.1 Physical model and boundary conditions

To ensure the stability of the solution and the continuity of the fluid field, the size of the particle should be smaller than that of the calculation grid [46]. As shown in Fig. 7, a grid model is built, and the boundary conditions are confirmed. Due to the large structural scale variation, tetrahedral grids are applied in the major computational domain, and the local mesh encryption method is adopted to improve the calculation accuracy in the constrained flow passage.

**Table 1** The coefficient table of erosion model

Coefficients	$k_1$	$k_3$	$s_1$	$s_2$	$q_1$	$q_2$	$\nu$	$D$
Value	- 0.05	0.19	0.71	0.14	2.8	- 1.00	99	326

**Table 2** Property sheet of workpiece material

Materials	TC4 titanium alloy	Monocrystalline silicon chip
Density (kg/m <sup>3</sup> )	4500	2320
Vickers hardness (GPa)	3.3	7

To validate the grid independence of the simulation results, three meshes are tested. Information on the number of cells used in the mesh studies is listed in Table 3. In all cases, the maximum fluid velocities in near-wall area are predicted by the three-phase computational model. And inspection of Table 3 indicates that the quantity of tetrahedral mesh cells has little effect on the simulation accuracy, and the maximum relative error is less than 3%. In this paper, mesh 2 is selected for the subsequent numerical simulations. The final mesh (mesh 2) resolutions on the polishing tool are depicted in Fig. 7.

For all numerical simulations, the boundary conditions are presented as follows: the inlet boundary condition uses the velocity inlet, the outlet boundary condition uses the pressure outflow, the wall condition adopts the no-slip boundary condition, the abrasive particle is SiC, and the distance between the CGLSP polishing tool and workpiece surface is 1 mm. We adopt the semi-implicit pressure-linked equations algorithm to address discrete pressure interpolation.

#### 4.2 Simulation results and analysis

According to the Preston equation, it can be inferred that the combined action of the dynamic pressure, fluid velocity, and turbulent kinetic energy of the near-wall surface determines the removal effect of the abrasive flow on the workpiece surface. The validation procedures are mainly performed around the abovementioned three key factors and the erosion behavior characteristics.

Figure 8 shows the simulation results of the velocity profile at the cross section of the model. From the contour of velocity, it can be seen that the velocity distribution range essentially covers the entire workpiece surface except for the central area. It is noteworthy that an obvious increasing velocity trend is found in the spiral area, in which the maximum fluid velocity is approximately 28 m/s. The trends of variation in dynamic pressure and turbulent kinetic energy are consistent with the fluid velocity shown in Figs. 9 and 10. The reason is that cavitation bubbles collapse in the fluid field, especially in the spiral area, causing explosive cavitation shock and high-velocity microjets. Therefore, when cavitation bubbles are introduced into the fluid flow field, the turbulent kinetic energy of the fluid and the random movement of abrasive particles can be enhanced.

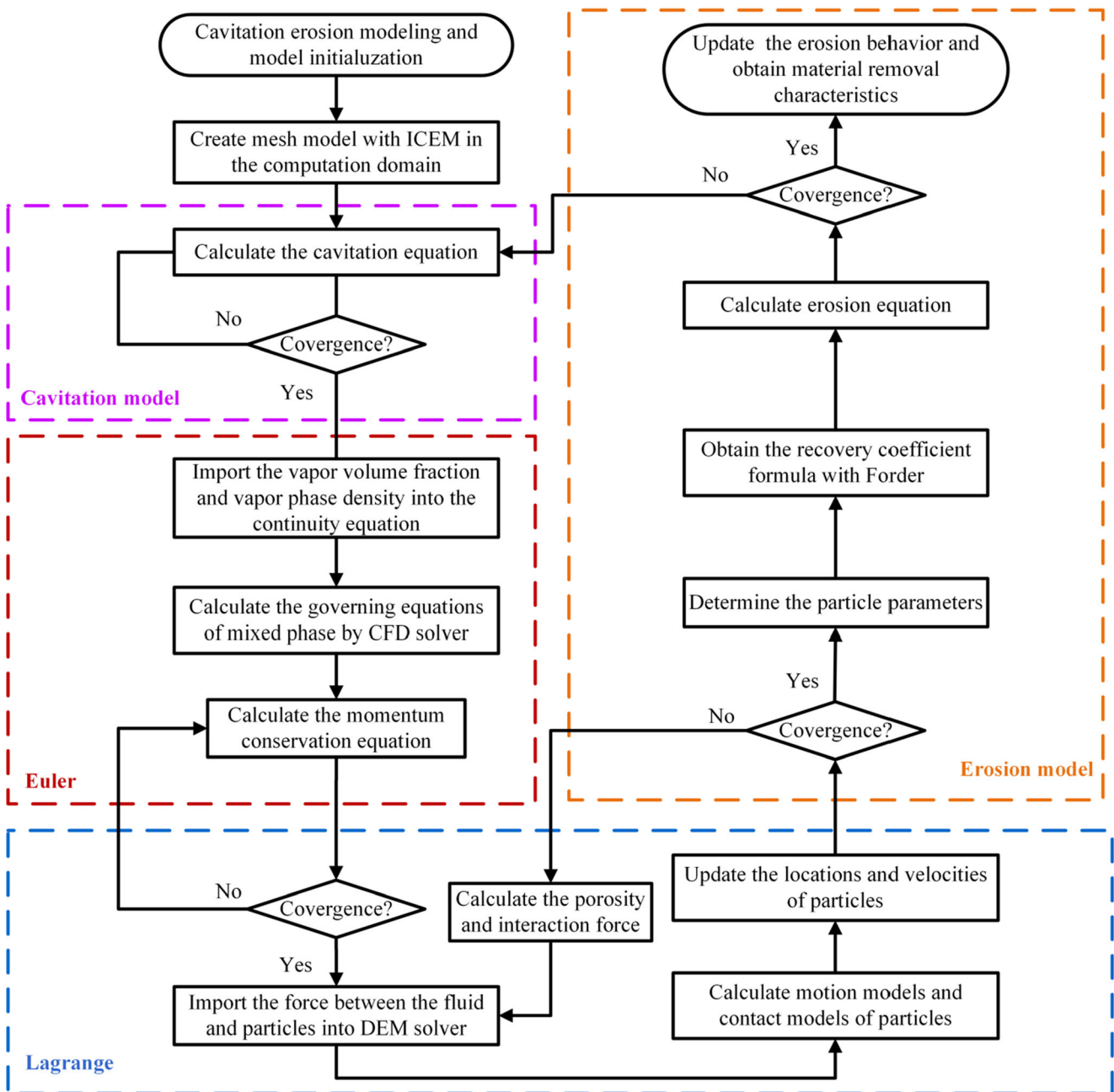


Fig. 6 Interphase coupling solution method for cavitation erosion

By analyzing the dynamic characteristics of the cavitation flow field, it can be suggested that the formation of cavitation effects will definitely affect the material removal mechanism for the CGLSP process. Considering the interplay of cavitating flow and particle motion, a simulation of the erosion model is conducted to predict the erosion rate and erosion depth of the workpiece surface in a polishing process.

The simulation is conducted on silicon wafers and TC4 titanium alloys, which are brittle and plastic materials, respectively. The corresponding cloud images of erosion rate for brittle and plastic materials are shown

in Fig. 11. The polished surface erosion rate  $R_{erosion}$  is given as:

$$R_{erosion} = \sum_{p=1}^{N_{particles}} \frac{m_p \cdot ER}{A_{face}} \tag{17}$$

$$ER = 1.0 \times 10^{-9} \rho_w E(\theta) \tag{18}$$

Here, ER is the erosion ratio, which is defined as the amount of mass loss of the polished surface material due to particle impacts divided by the mass of particles impacting;  $\rho_w$



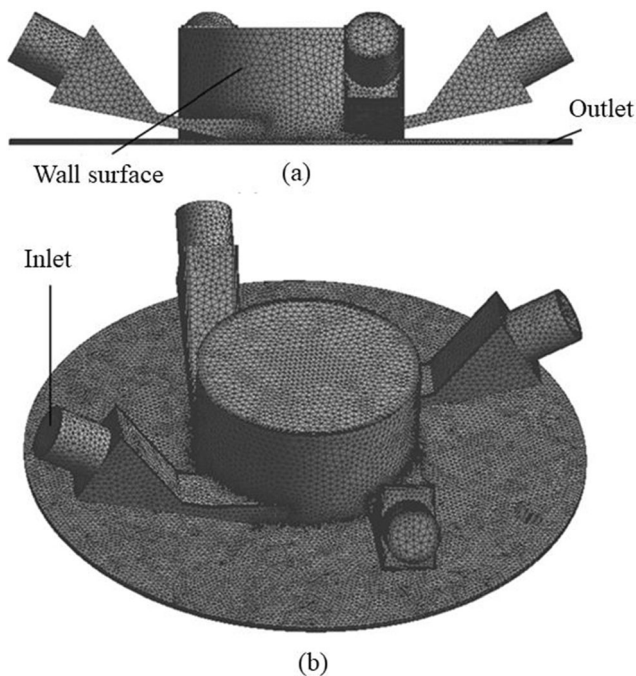


**Fig. 7** Mesh generation and boundary conditions. **a** Front view. **b** Axonometric

is the density of the polished surface materials, which are silicon wafer and TC4 titanium alloy;  $A_{face}$  is the area of the cell face at the wall; and  $m$  represents the mass rate of particles impacting the cell surface. As shown in Fig. 11, the gas-liquid-solid abrasive flow in the spiral area leads to severe erosion due to high particle impact velocities compared to those in the auxiliary processing area and vacuum area. This is because in the spiral area, in addition to the leading role of the fluid phase, particle motion is strongly affected by cavitation bubble collapse, resulting in the improvement of the kinetic energy of the fluid and the enhancement of abrasive particle movement.

The curves of the predicted erosion rate distribution for brittle-plastic materials are shown in Fig. 12. The erosion rate shows an increasing trend with the enhancement of the cavitation erosion effect in the entire fluid field. This implies that the spiral area will be the maximum material removal part, while other parts will suffer a lower removal rate due to the lack of an obvious effect of cavitation effects. Comparing the simulated results of the two materials, the maximum erosion rate on the TC4 titanium alloy is larger than that of the silicon wafer under the same polishing conditions. The reason is that

the hardness of the silicon wafer is larger than that of the TC4 titanium alloy. It is also observed that the variation curve of the predicted erosion rate distribution basically indicates an M-shaped pattern, which is similar to the material removal rules of other SAF polishing methods.

With the result of the predicted erosion rate, the rate of the erosion depth  $ER_{depth}$  is calculated as:

$$ER_{depth} = \sum_{p=1}^{N_{particles}} \frac{\dot{m}_p ER}{A_{face} \rho_w} \tag{19}$$

Here,  $\rho_w$  is the density of the target surface material. Following a period of fixed-point processing ( $T$ ), the erosion depth can be given as:

$$ED = \frac{R_{erosion}}{\rho_w} \cdot T \tag{20}$$

Figure 13 shows the predicted erosion depth distribution for different materials according to Eq. (20). As can be observed in this figure, the predicted erosion depth shows an increasing trend with an enhancing cavitation erosion effect, which is consistent with the trend of the predicted erosion rate. Another important point to note about this figure is that the maximum erosion depth occurs in the spiral area where the cavitation effects are quite intense, and hence, the material removal rate in the spiral area is much greater than that in the other area on the polished surface during a polishing process. Thus, it is hypothesized that the CGLSP technique could realize a much higher quality surface and polishing efficiency than SAF processing.

With the information in Fig. 13, it can be seen that the material removal function presents a W-shaped distribution. To achieve material homogenization removal for large workpieces, the material removal curve on the adjacent polishing path should have a certain degree of cumulative superposition. Based on Eq. (20), the erosion depth function is related to dwell time and material density; thus, the maximum erosion depth and the corresponding position remain unchanged when selecting the different dwell point spacings. Taking the processing process for silicon chips as an example, the relationship between reasonable dwell spacing points and the erosion depth function is discussed. A schematic diagram of the dwell point spacing is shown in Fig. 14, in which three erosion depth curves are represented. The offset between the adjacent two erosion depth curves is defined as the dwell point spacing. Theoretically, when the two curves intersect at 1/2 of the maximum erosion depth ( $2M_0 = M_d$ ), a uniform surface can be obtained, and the processing efficiency can be greatly improved. A reasonable dwell point spacing can be obtained through analysis as follows:

$$d = 2|x_0| \tag{21}$$

**Table 3** Grid independent verification

Mesh #	Mesh cells	Velocity (m/s)	Relative error
1	620464	29.6	—
2	845682	30.2	1.5%
3	1003682	30.6	2.5%

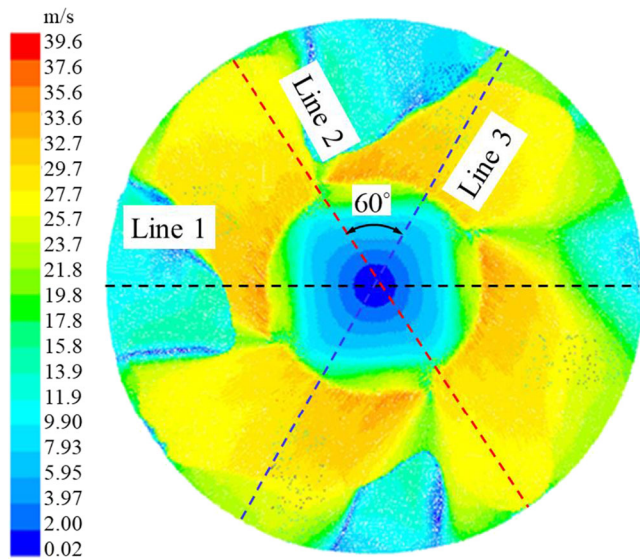


Fig. 8 Simulated fluid velocity profile at the cross section

Here,  $d$  is the dwell point spacing, and  $x_0$  is the  $x$ -value when the two curves intersect at  $1/2$  of the maximum erosion depth, which can be obtained through numerical simulation. To improve the surface quality, reasonable dwell point spacing for two different materials is employed in the processing experiments.

## 5 Experiment and result discussion

### 5.1 CGLSP experimental platform

To identify the effectiveness of the proposed method and polishing tool, a CGLSP experimental platform is set up [47,

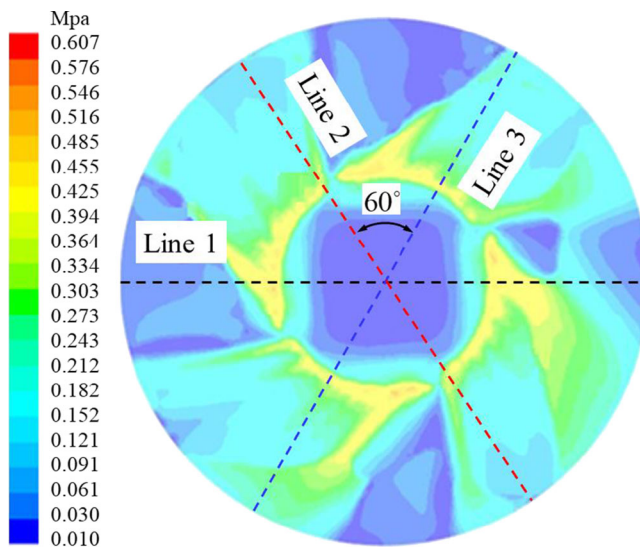
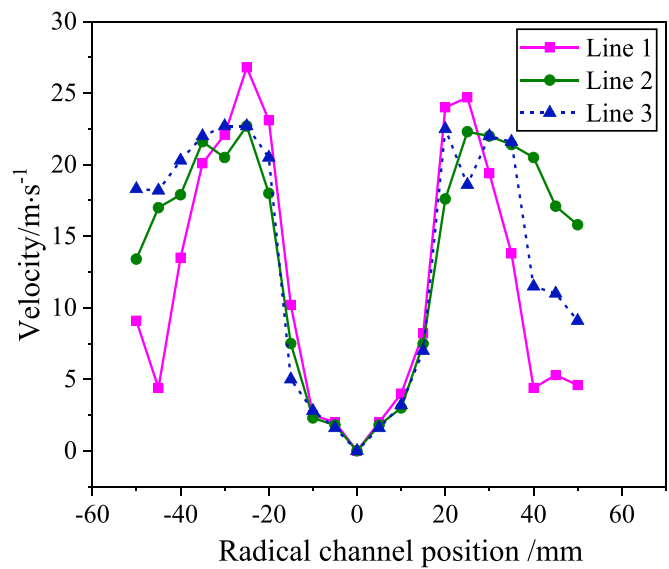
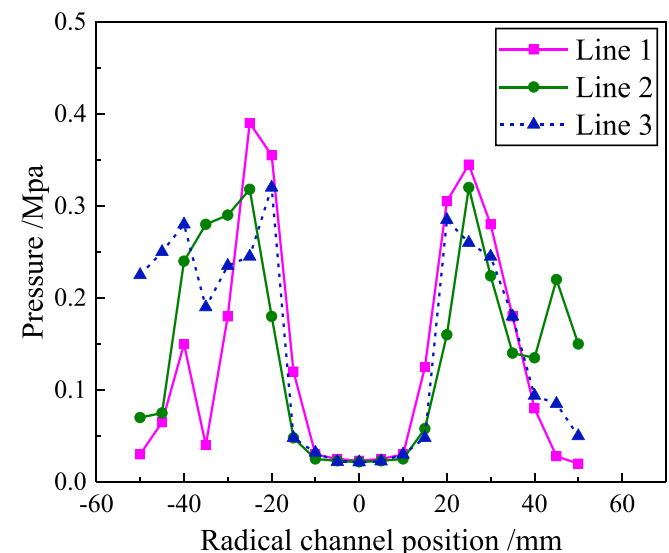


Fig. 9 Simulated pressure profile at the cross section



48] as shown in Fig. 15. The abrasive particles and deionized water are well mixed in the tank to form a liquid-solid two-phase flow. Then, the mixed medium is injected into the polishing tool after passing through the manometer and flowmeter [49]. The fluid flow state during processing is monitored through the valve, pressure gauge, and flowmeter. Meanwhile, the work of the processing process is controlled by the control system [50–52].

Corresponding to the simulation experiment, the work-piece materials used in this experiment are silicon wafer and TC4 titanium alloy. The 4000# SiC abrasive combined with deionized water is used as the polishing slurry, with particles of an average size of  $3.2 \mu\text{m}$ . It should be noted that the SiC abrasive particles are brittle materials, and they experience no phase transition during the polishing process [53].



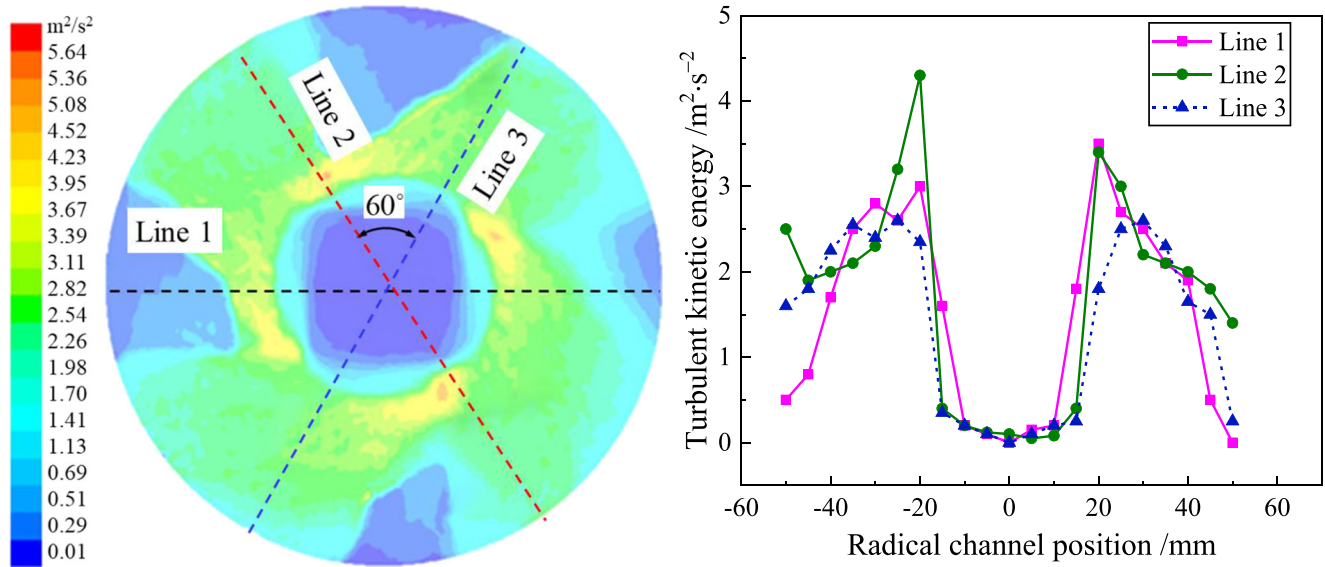


Fig. 10 Simulated turbulent kinetic energy profile at the cross section

### 5.2 Experimental results and discussion

Based on the above experimental platform, two groups of processing experiments are conducted. In addition to abrasive particles, cavitation bubbles are generated by the constrained fluid channel during the processing process to erode the workpiece surface. As a result of controlled polishing due to cavitation erosion-aided abrasion, large stock material from the workpiece surface including larger sized irregularities can be removed during the CGLSP process.

As seen in Fig. 16, the predicted erosion depth profiles are compared with the experimental profile for different materials. The left part of each figure in Fig. 16 is the comparison of

practical and simulation erosion depths, while the right part is the deviation between them. It is noted that the practical erosion depths for plastic-brittle materials agree reasonably well with the predicted results, which validates the effectiveness of the proposed computational modeling approach. However, influenced by the measurement errors and the precision of the processing tool, the practically generated erosion depth profile does not conform with the predicted results in vacuum areas and spiral areas. This is the main reason for the deviation between the simulation and experimental results. In addition, there are some assumptions made in the cavitation erosion model mentioned in Section 3, resulting in differences between the predicted and experimental results. In subsequent

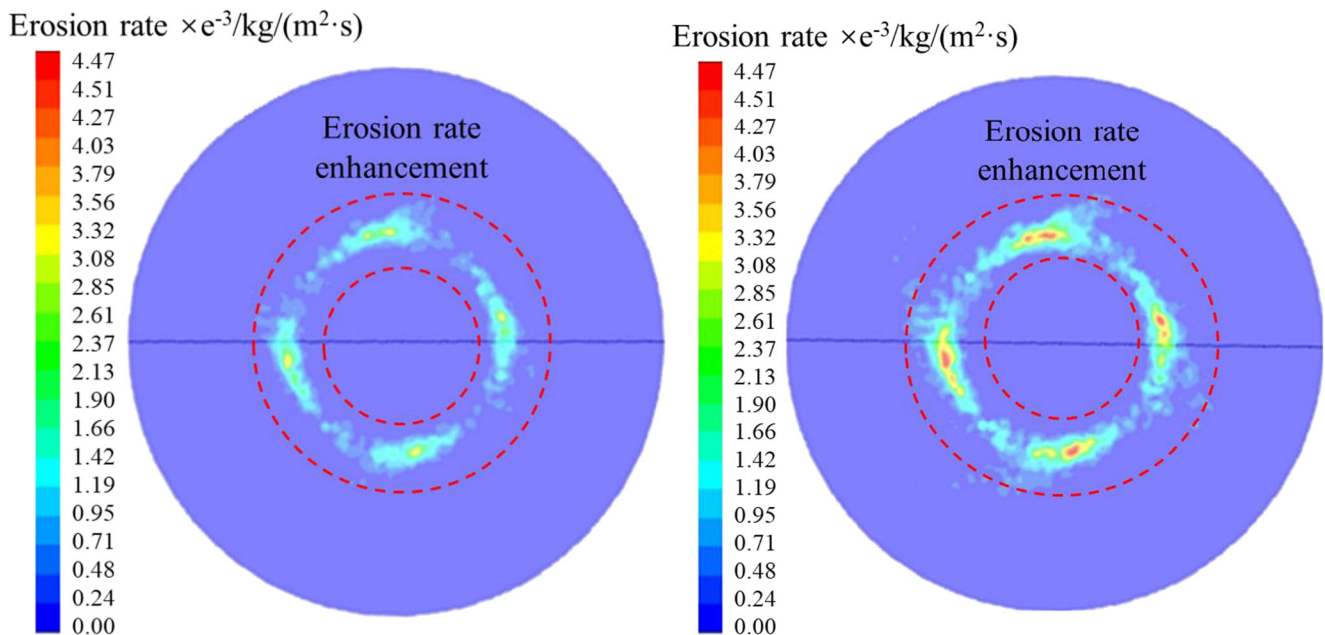
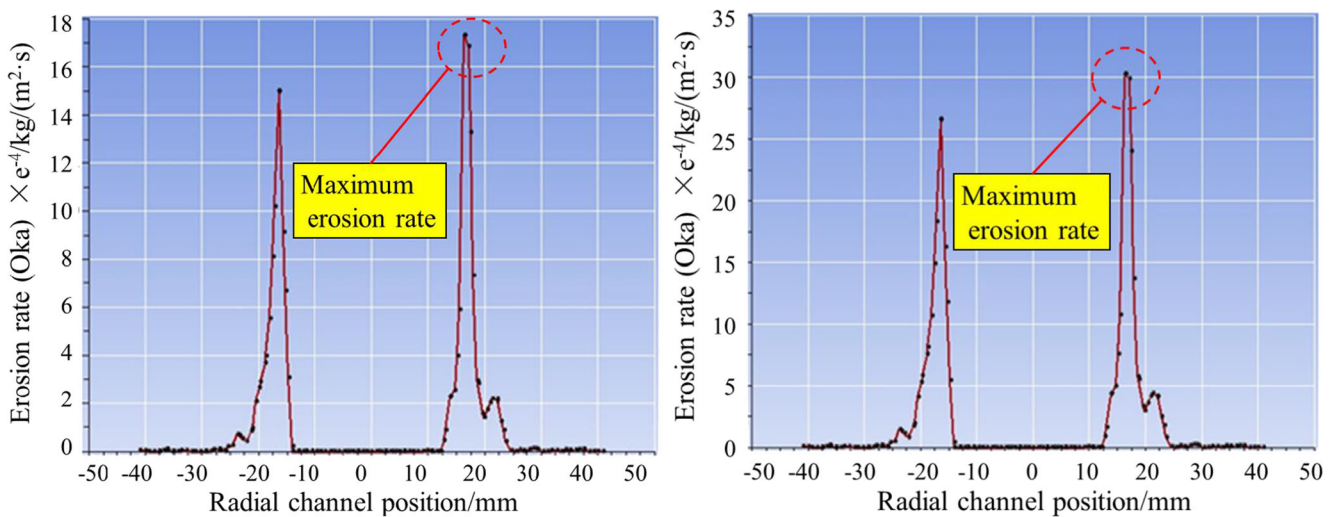


Fig. 11 Cloud images of erosion velocity on different material surfaces. a Polishing on silicon wafer. b Polishing on TC4 titanium alloy



**Fig. 12** Predicted erosion rate distribution of different materials. **a** Polishing on silicon wafer. **b** Polishing on TC4 titanium alloy

research, to reduce related errors, relevant empirical parameters should be modified according to the practical processing conditions.

To further validate the potential impact of the CGLSP process on the material removal mechanism of brittle-plastic materials, the polished surface texture is examined with scanning electron microscopy (SEM) [54]. In-situ SEM observation is performed in the same region of the cross-section surface of the two materials after the polishing process to acquire more detailed information on the material removal mechanism in CGLSP process. Figure 17 clearly shows the surface microstructures of the TC4 titanium alloy and silicon wafer before the polishing process, particularly the locations highlighted by rectangles and circles. As shown in Fig. 17a, numerous fractures with considerable damage zones and residual microcracks can be found in the original workpiece surface of TC4 titanium alloy. Because of its high strength and high

compactness, residual pores and massive structures are evident on the original surface of the silicon wafer, as shown in Fig. 17b. It has been reported that cavitation erosion initially occurs at or around pre-existing pores and cracks and then increases during the cavitation erosion process [55]. Therefore, these surface irregularities present in the polished surface can be preferentially eroded in polishing process.

Based on SEM observations, a conceptual representation of the material removal mechanism in the CGLSP process is presented. Figures 18 and 19 clearly show the microstructural transformation of the TC4 titanium alloy and silicon wafer, respectively. The primary erosion mechanism that contributes to material removal is of interest in this study. Compared with the original polished surface, it is apparent that the surface quality for brittle-plastic materials is improved greatly by means of the CGLSP process. When processed for 0.5 h, as seen in Fig. 18a and b, there are still some obvious

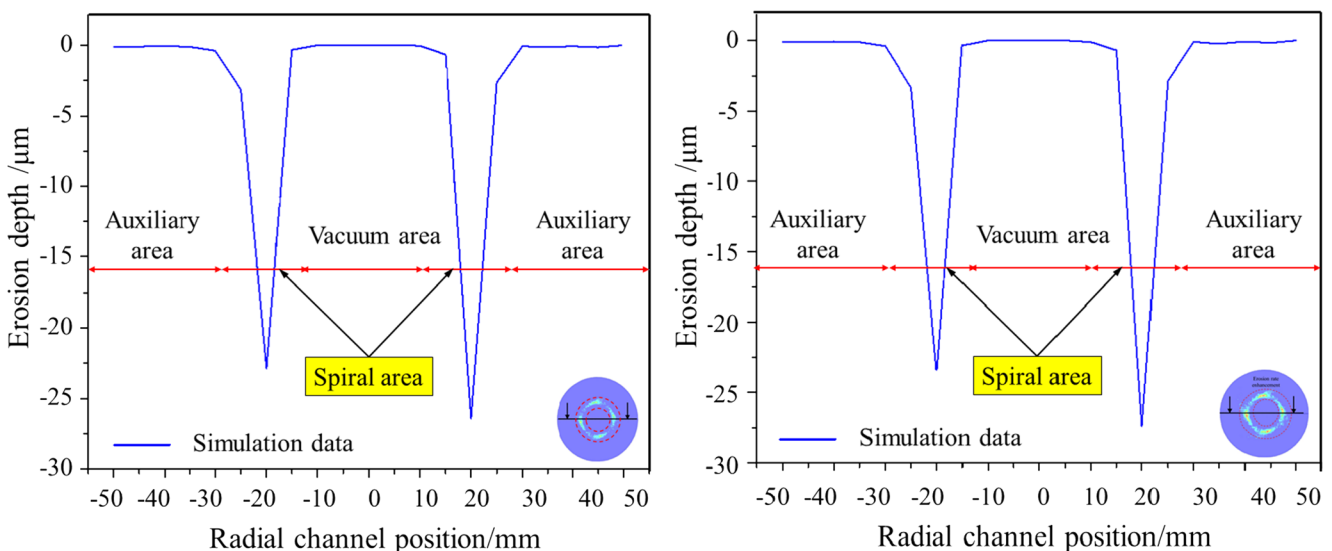
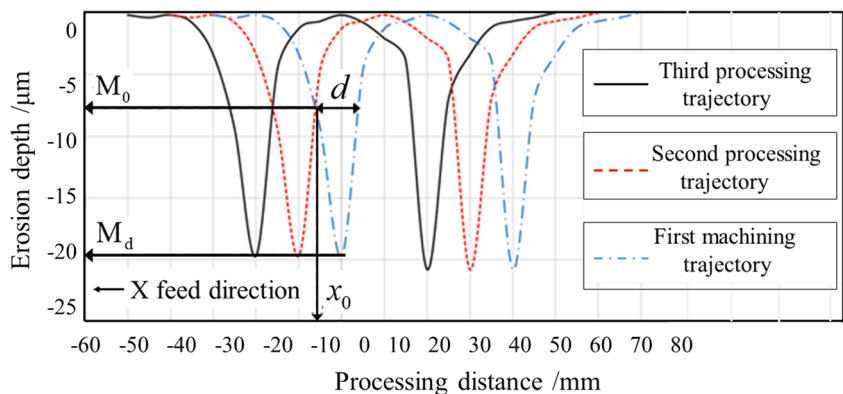


**Fig. 13** Predicted erosion depth distribution of different materials. **a** Polishing on silicon wafer. **b** Polishing on TC4 titanium alloy

Fig. 14 Schematic diagram of dwell point spacing selection



microcracks and damage zones in the polished surface. Material removal is not observed on the polished surface, and no improvements in polished surface quality are achieved during the initial polishing phase. With a further increase in the polishing time to 2 h, the crack areas show a significant reduction and begin to form a relatively smooth surface, as shown in Fig. 18c and d. Hence, the removal of larger irregularities depends mainly on the polishing time. Similarly, when polished for 0.5 h and further to 2 h, pores and massive structures are eroded, and the polished surface of the silicon wafer is improved to some extent, as shown in Fig. 19. An increase in the cavitation erosion effect can result in the further removal of surface irregularities and smooth the entire polished surface of the workpiece. Inspection of the SEM morphology (Figs. 18 and 19) indicates that cavitation erosion effects initially occur around pre-existing pores and cracks. The shock waves due to cavitation bubble collapse that act on the polished surface have the noticeable effect of causing the reduction of pores and microcracks. As a result of controlled polishing because of cavitation erosion and the presence of abrasive particles, larger irregularities from the workpiece surface, including pores and microcracks, can be removed, and a better surface quality is obtained. According

to the topography analyses, the material removal mechanism due to cavitation erosion aided by abrasive particles in three-phase flows is illustrated, and the effectiveness of the CGLSP method is validated.

### 6 Conclusions

To overcome the low material removal rate of soft abrasive flow (SAF) for large workpieces, a cavitation-based gas-liquid-solid abrasive flow polishing (CGLSP) process is proposed. The corresponding computational modeling method and processing experiments are performed to reveal the material removal mechanism, and the main conclusions are as follows:

- 1) Through a surface-constrained module, a polishing tool constructed using a multi-inlet constrained fluid channel for brittle-plastic material processing is designed in which bubbles are generated into the abrasive flow to enhance the processing efficiency.
- 2) Based on an Eulerian-Lagrangian framework, cavitation model, and Oka erosion model, a coupling computational fluid dynamics model is built, and realistic erosion prediction results are produced.
- 3) The simulated results reveal that erosion of the workpiece surface mainly occurs in the spiral area of the polishing tool; the predicted erosion rate and erosion depth show an increasing trend with increasing of cavitation intensity; homogenized material removal for large workpieces can be achieved by selecting a reasonable dwell point spacing.
- 4) A CGLSP polishing platform is set up, and extensive experiments are conducted. The experimental results show that the proposed CGLSP method can realize a much higher quality surface and polishing efficiency on large workpieces.

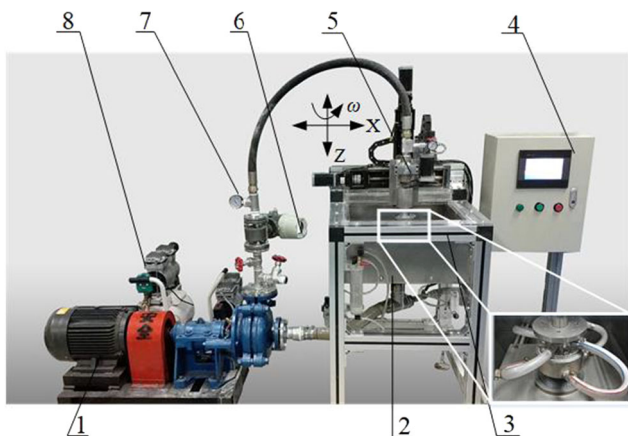
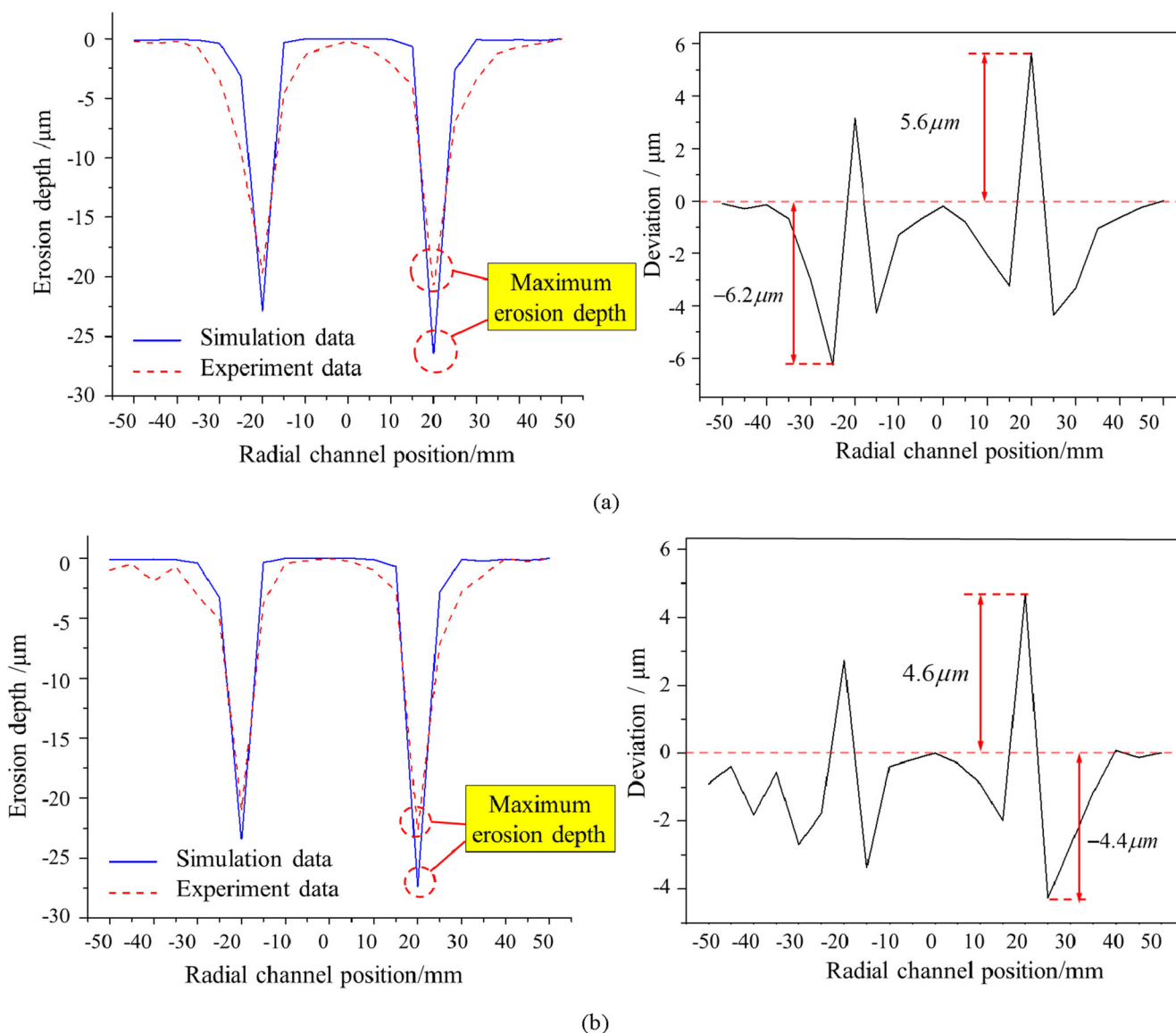


Fig. 15 CGLSP experimental platform. 1, booster pump; 2, abrasive flow tank; 3, experiment platform; 4, control cabinet; 5, sports platform; 6, flowmeter; 7, manometer; 8, gas source

In general, this research not only proposes a computational modeling method to predict the potential effect of cavitation



**Fig. 16** Comparison of erosion depth between the experiment and simulation results. **a** Erosion depth of the polishing on silicon wafer. **b** Erosion depth of the polishing on TC4 titanium alloy

erosion on the CGLSP technique but also reveals the material removal mechanism during polishing through a series of experiments. Subsequent research will be performed on the design of highly erosion-resistant polishing tools and the effect of abrasive hardness on the material removal process.

**Nomenclature**  $\rho_v$ , Vapor phase density;  $\rho_l$ , Liquid phase density;  $\alpha_v$ , Vapor phase volume fraction;  $\alpha_l$ , Liquid phase volume fraction;  $\mathbf{u}$ , Velocity vector;  $\mu$ , Dynamic viscosity;  $\mathbf{F}$ , Reaction force of discrete particles relative to continuous phase in unit volume;  $t$ , Time;  $F_d$ , Drag force;  $F_{other}$ , Force acting on particles;  $\mathbf{u}_p$ , Particle velocity;  $\mathbf{g}$ , Gravitational acceleration;  $\rho_p$ , Particle density;  $\rho_w$ , Water density;  $N$ , Number of particles per unit time;  $m_p$ , Mass of the particle;  $v$ , Impact velocity of the particle;  $\mu_1$ , Dynamic viscosity;  $R_b$ , Radius of vacuole;  $R_c$ , Radius of condensation phase;  $R_e$ , Radius of evaporation phase;  $P_e$ , Local pressure of the fluid;

$P_b$ , Bubble surface pressure;  $P$ , Medium pressure in the flow field;  $P_v$ , Saturated vapor pressure of the medium;  $n_b$ , Number of bubbles in a unit liquid volume;  $v_r$ , Rebound velocity;  $v_{in}$ , Incoming velocity;  $e_n$ , Normal recovery coefficient;  $e_t$ , Tangential recovery coefficient;  $\theta$ , Impact angle;  $E(\theta)$ , A unit of material volume removed per mass of particles;  $n_1, n_2$ , Exponents;  $s_1, s_2, q_1, q_2$ , Fitting constants;  $K$ , Particle property factor;  $k_1, k_2, k_3$ , Exponent factors;  $R_{erosion}$ , Erosion rate; ER, Erosion ratio;  $\rho_w$ , Density of the target surface materials;  $A_{face}$ , Erosion area;  $m$ , Mass rate of particles impacting the cell surface; ER<sub>depth</sub>, Rate of the erosion depth;  $T$ , A period of fixed-point processing;  $d$ , Dwell point spacing;  $x_0$ , x-value

**Code availability** Not applicable.

**Authors' contributions** Man Ge is responsible for methodology, investigation, software, writing, and editing. Shiming Ji and Dapeng Tan are responsible for funding support, algorithm implementation, supervision, and validation. Huiqiang Cao is responsible for methodology discussion and manuscript refinement.

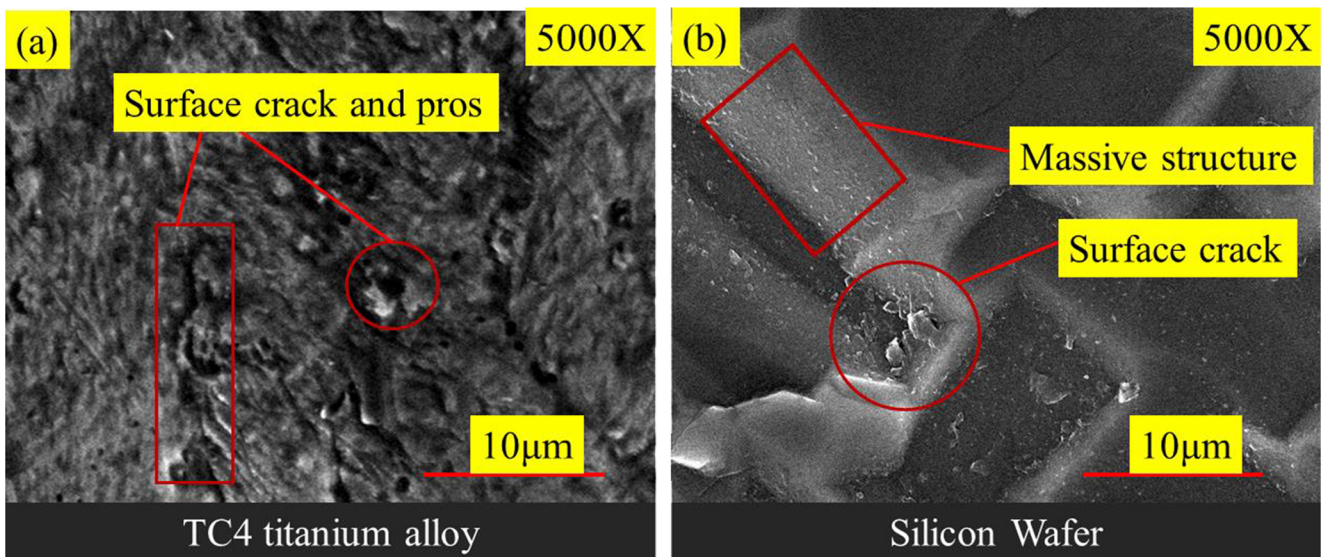


Fig. 17 The original surface of brittle-plastic materials. **a** TC4 titanium alloy (×5000). **b** Silicon wafer (×5000)

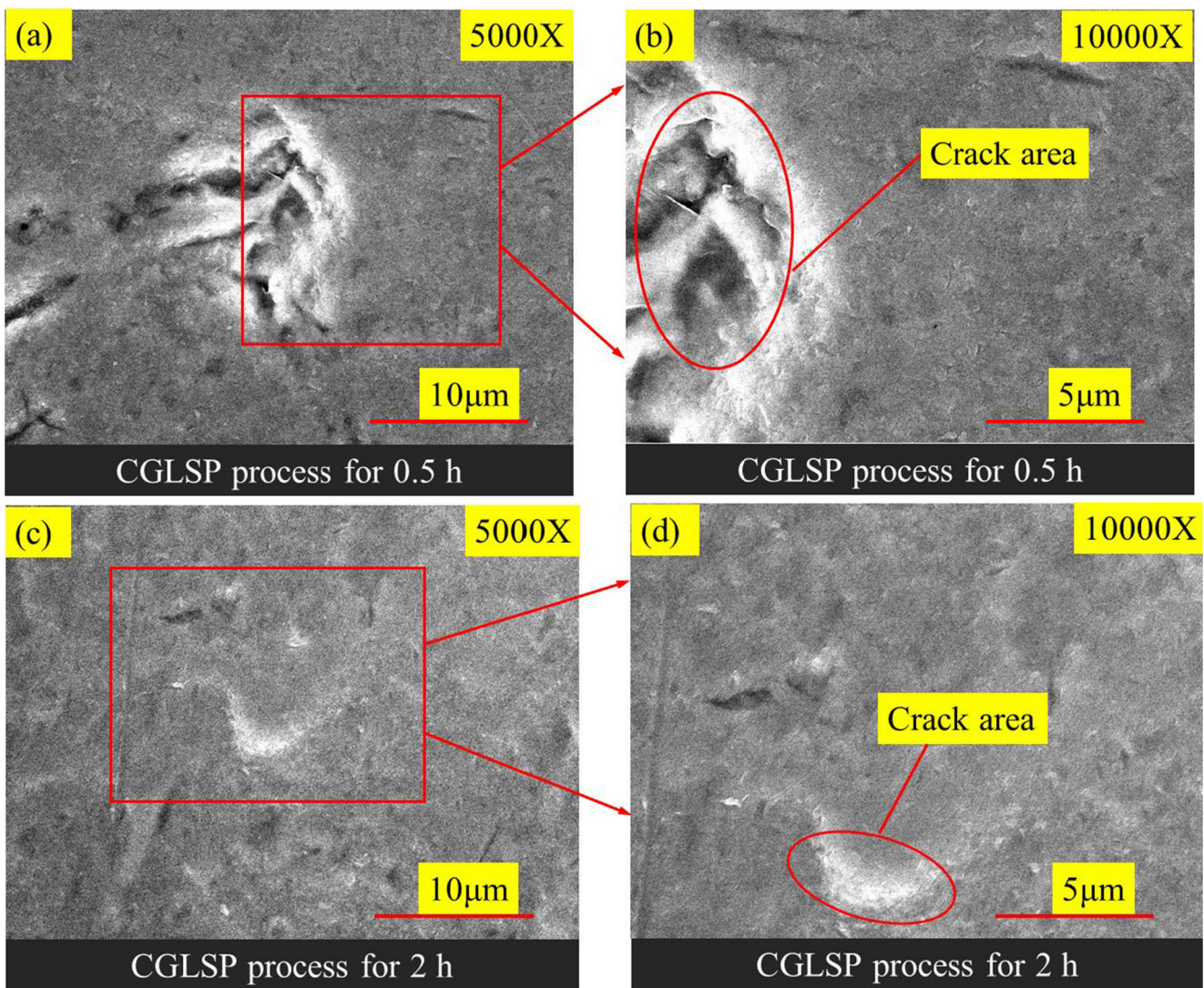
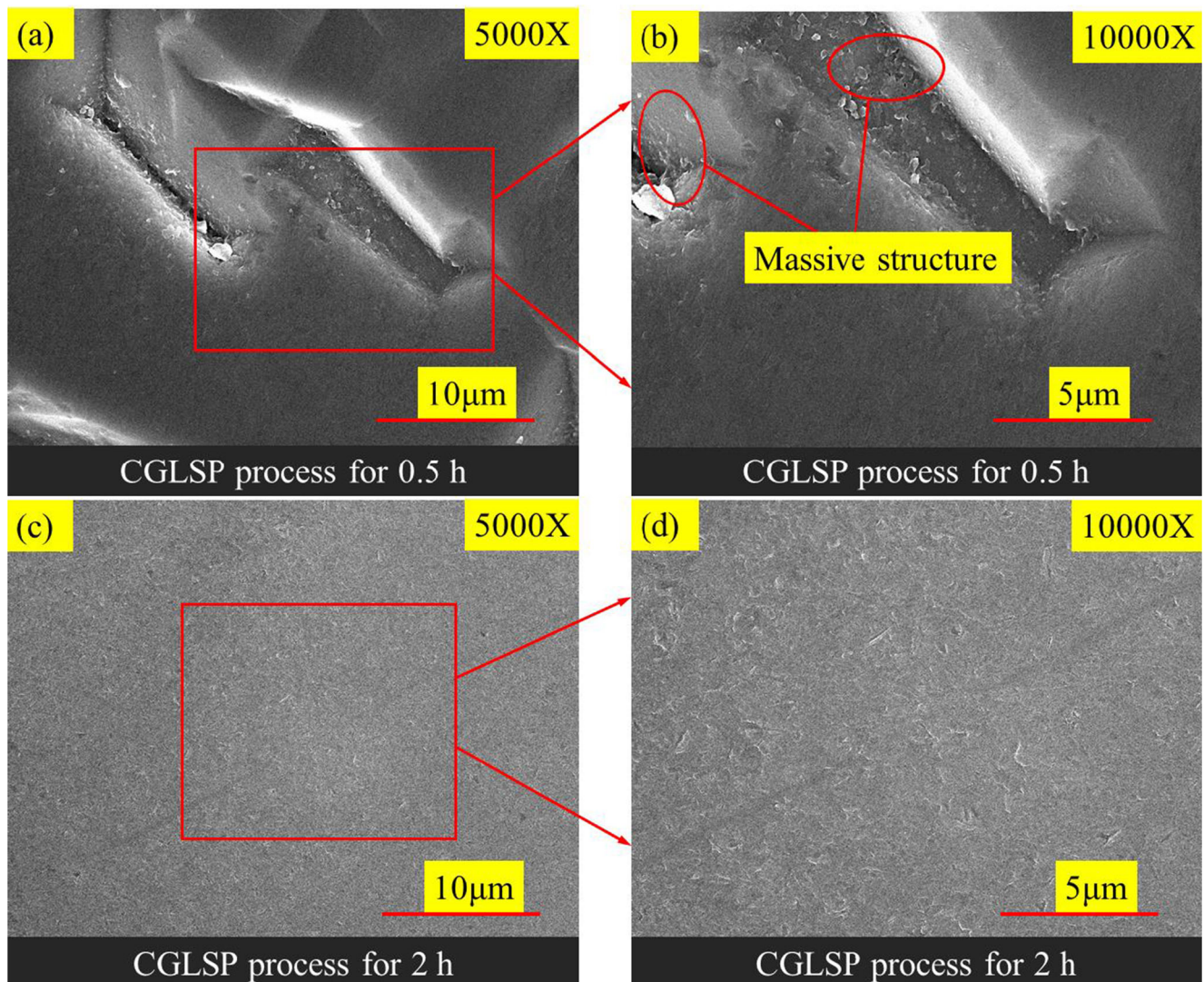


Fig. 18 SEM topography of TC4 titanium alloy polished surface. **a** Polishing for 0.5 h (5000). **b** Polishing for 0.5 h (×10,000). **c** Polishing for 2 h (×5000). **d** Polishing for 0.5 h (×5000)



**Fig. 19** SEM topography of silicon wafer polished surface. **a** Polishing for 0.5 h ( $\times 5000$ ). **b** Polishing for 0.5 h ( $\times 10,000$ ). **c** Polishing for 2 h ( $\times 5000$ ). **d** Polishing for 2 h ( $\times 10,000$ )

**Funding** This work was supported by the Natural Science Foundation of China under Grant Nos. 51775501 and 51575494, the Natural Science Foundation of Zhejiang Province under Grant No. LR16E050001.

**Data availability** The datasets and materials used or analyzed during the current study are available from the corresponding author on reasonable request.

## Declarations

**Ethical approval** All authors confirm that they follow all ethical guidelines.

**Consent to participate** Not applicable.

**Consent to publish** The manuscript is approved by all authors for publication; all the authors listed have approved the manuscript that is enclosed.

**Conflict of interest** The authors declare no conflict of interest.

## References

1. Beaucamp A, Namba Y (2013) Super-smooth finishing of diamond turned hard X-ray molding dies by combined fluid jet and bonnet polishing. *CIRP Annals* 62(1):315–318
2. Wang CJ, Cheung CF, Ho LT, Liu MY, Lee WB (2017) A novel multi-jet polishing process and tool for high-efficiency polishing. *Int J Mach Tools Manuf* 115:60–73
3. Fu Y, Gao H, Yan Q, Wang X, Wang X (2020) Rheological characterisation of abrasive media and finishing behaviours in abrasive flow machining. *Int J Adv Manuf Technol* 107(7):3569–3580
4. Ge JQ, Li C, Gao ZY, Ren YL, Xu XS, Li C, Xie Y (2021) Softness abrasive flow polishing method using constrained boundary vibration. *Powder Technol* 382:173–187
5. Ji SM, Tang B, Tan DP, Gong B, Yuan Q, Pan Y (2010) Structured surface softness abrasive flow precision finish machining and its



- abrasive flow dynamic numerical analysis. *Chinese J Mech Eng* 46(15):178–184
6. Zhao J, Jiang EY, Qi H, Ji SM, Chen Z (2020) A novel polishing method for single-crystal silicon using the cavitation rotary abrasive flow. *Precis Eng* 61:72–81
  7. Zhao J, Huang JF, Wang R, Peng HR, Ji SM (2020) Investigation of the optimal parameters for the surface finish of K9 optical glass using a soft abrasive rotary flow polishing process. *J Manuf Process* 49:26–34
  8. Ravi Sankar M, Jain VK, Ramkumar J, Joshi YM (2011) Rheological characterization of styrene-butadiene based medium and its finishing performance using rotational abrasive flow finishing process. *Int J Mach Tools Manuf* 51(12):947–957
  9. Li C, Ji SM, Tan DP (2012) Softness abrasive flow method oriented to tiny scale mold structural surface. *Int J Adv Manuf Technol* 61(9-12):975–987
  10. Tan DP, Ji SM, Fu YZ (2016) An improved soft abrasive flow finishing method based on fluid collision theory. *Int J Adv Manuf Technol* 85(5-8):1261–1274
  11. Chen HS, Li J, Chen DR, Wang JD (2008) Damages on steel surface at the incubation stage of the vibration cavitation erosion in water. *Wear* 265(5-6):692–698
  12. Brujan EA, Takahira H, Ogasawara T (2019) Planar jets in collapsing cavitation bubbles. *Exp Therm Fluid Sci* 101:48–61
  13. Chen F, Miao X, Tang Y, Yin S (2017) A review on recent advances in machining methods based on abrasive jet polishing (AJP). *Int J Adv Manuf Technol* 90(1):785–799
  14. Zhang L, Wang JS, Tan DP, Yuan ZM (2017) Gas compensation-based abrasive flow processing method for complex titanium alloy surfaces. *Int J Adv Manuf Technol* 92:3385–3397
  15. Ge JQ, Ji SM, Tan DP (2018) A gas-liquid-solid three-phase abrasive flow processing method based on bubble collapsing. *Int J Adv Manuf Technol* 95(1-4):1069–1085
  16. Sreedhar BK, Albert SK, Pandit AB (2017) Cavitation damage: Theory and measurements – a review. *Wear* 372-373:177–196
  17. Beaucamp A, Katsura T, Takata K (2018) Process mechanism in ultrasonic cavitation assisted fluid jet polishing. *CIRP Annals* 67(1):361–364
  18. Ge JQ, Ren YL, Xu XS, Li C, Li ZA, Xiang WF (2021) Numerical and experimental study on the ultrasonic-assisted soft abrasive flow polishing characteristics. *Int J Adv Manuf Technol* 112(4):1–19
  19. Toh CK (2007) The use of ultrasonic cavitation peening to improve micro-burr-free surfaces. *Int J Adv Manuf Technol* 31(7):688–693
  20. Li L, Qi H, Yin ZC, Li DF, Zhu ZL, Tangwarodomnukun V, Tan DP (2020) Investigation on the multiphase sink vortex Ekman pumping effects by CFD-DEM coupling method. *Powder Technol* 360:462–480
  21. Tang T, Gao L, Li B, Liao L, Xi Y, Yang G (2019) Cavitation optimization of a throttle orifice plate based on three-dimensional genetic algorithm and topology optimization. *Struct Multidiscip Optim* 60(3):1227–1244
  22. Hosbach M, Skoda R, Sander T, Leuteritz U, Pfitzner M (2020) On the temperature influence on cavitation erosion in micro-channels. *Exp Therm Fluid Sci* 117:110140
  23. Ansari MA, Samanta A, Behnagh RA, Ding H (2019) An efficient coupled Eulerian-Lagrangian finite element model for friction stir processing. *Int J Adv Manuf Technol* 101(5):1495–1508
  24. Zheng SH, Yu YK, Qiu MZ, Wang LM, Tan DP (2021) A modal analysis of vibration response of a cracked fluid-filled cylindrical shell. *Appl Math Model* 91:934–958
  25. Nguyen VB, Nguyen QB, Zhang YW, Lim CYH, Khoo BC (2016) Effect of particle size on erosion characteristics. *Wear* 348-349:126–137
  26. Duarte CAR, de Souza FJ (2017) Innovative pipe wall design to mitigate elbow erosion: A CFD analysis. *Wear* 380-381:176–190
  27. Messa GV, Malavasi S (2018) A CFD-based method for slurry erosion prediction. *Wear* 398-399:127–145
  28. Zahedi P, Zhang J, Arabnejad H, McLaury BS, Shirazi SA (2017) CFD simulation of multiphase flows and erosion predictions under annular flow and low liquid loading conditions. *Wear* 376-377:1260–1270
  29. Ji SM, Cao HQ, Zhao J, Pan Y, Jiang EY (2018) Soft abrasive flow polishing based on the cavitation effect. *Int J Adv Manuf Technol* 101(5-8):1865–1878
  30. Ge JQ, Ji SM, Tan DP (2017) A gas-liquid-solid three-phase abrasive flow processing method based on bubble collapsing. *Int J Adv Manuf Technol* 95(1-4):1069–1085
  31. Li L, Lu JF, Fang H, Yin ZC, Wang T, Wang RH, Fan XH, Zhao LJ, Tan DP, Wan YH (2020) Lattice Boltzmann method for fluid-thermal systems: status, hotspots, trends and outlook. *IEEE Access* 8:27649–27675
  32. Tan DP, Li L, Zhu YL, Zheng S, Yin ZC, Li DF (2019) Critical penetration condition and Ekman suction-extraction mechanism of a sink vortex. *J Zhejiang Univ - SCI A* 20(1):61–72
  33. Ji SM, Weng XX, Tan DP (2012) Analytical method of softness abrasive two-phase flow field based on 2D model of LSM. *Acta Physica Sinica* 61(1):7
  34. Zeng X, Ji SM, Tan DP, Jin MS, Wen DH, Zhang L (2013) Softness consolidation abrasives material removal characteristic oriented to laser hardening surface. *Int J Adv Manuf Technol* 69(9-12):2323–2332
  35. Fan XH, Tan DP, Li L, Yin ZC, Wang T (2021) Hybrid modeling and solution method of gas-liquid-solid three-phase particle flow. *Acta Phys Sin (Article in press)*
  36. Tan DP, Li L, Yin ZC, Li DF, Zhu YL, Zheng S (2020) Ekman boundary layer mass transfer mechanism of free sink vortex. *Int J Heat Mass Transf* 150:119250
  37. Tan DP, Yang T, Zhao J, Ji SM (2016) Free sink vortex Ekman suction-extraction evolution mechanism. *Acta Physica Sinica* 65(5):12
  38. Zhao J, Huang JF, Xiang YC, Wang R, Xu XQ, Ji SM, Hang W (2021) Effect of a protective coating on the surface integrity of a microchannel produced by microultrasonic machining. *J Manuf Processes* 61:280–295
  39. Di Felice R (1994) The voidage function for fluid-particle interaction systems. *Int J Multiphase Flow* 20(1):153–159
  40. Rayleigh L (1917) On the pressure developed in a liquid during the collapse of a spherical cavity. *Philos Mag* 34(200):94–98
  41. Sauer J (2001) Schnerr GH (2000) Development of a new cavitation model based on bubble dynamics. *Z Angew Math Mech* 81:561–562
  42. Feng X, Lu J (2019) Effects of balanced skew and biased skew on the cavitation characteristics and pressure fluctuations of the marine propeller. *Ocean Eng* 184:184–192
  43. Forder A, Thew M, Harrison D (1998) A numerical investigation of solid particle erosion experienced within oilfield control valves. *Wear* 216(2):184–193
  44. Oka YI, Okamura K, Yoshida T (2005) Practical estimation of erosion damage caused by solid particle impact: Part 1: Effects of impact parameters on a predictive equation. *Wear* 259(1):95–101
  45. Zhang Y, Reuterfors EP, McLaury BS, Shirazi SA, Rybicki EF (2007) Comparison of computed and measured particle velocities and erosion in water and air flows. *Wear* 263:330–338
  46. Farokhipour A, Mansoori Z, Saffar-Avval M, Ahmadi G (2020) 3D computational modeling of sand erosion in gas-liquid-particle multiphase annular flows in bends. *Wear* 450-451:203241
  47. Li L, Tan DP, Wang T, Yin ZC, Fan XH, Wang RH (2021) Multiphase coupling mechanism of free surface vortex and the vibration-based sensing method. *Energy* 216:119136

48. Zhang LB, Lv HP, Tan DP, Xu F, Chen JL, Bao GJ, Cai SB (2018) Adaptive quantum genetic algorithm for task sequence planning of complex assembly systems. *Electron Lett* 54(14):870–871
49. Tan DP, Ni YS, Zhang LB (2017) Two-phase sink vortex suction mechanism and penetration dynamic characteristics in ladle teeming process. *J Iron Steel Res Int* 24(7):669–677
50. Wang JX, Gao SB, Tang ZJ, Tan DP, Cao B, Fan J (2021) A context-aware recommendation system for improving manufacturing process modeling. *J Intell Manuf* (Article in press)
51. Wang JX, Cao B, Zheng X, Tan DP, Fan J (2019) Detecting difference between process models using edge network. *IEEE Access* PP(99):1–1
52. Jiang QS, Tan DP, Li YB, Ji SM, Cai CP, Zheng QM (2020) Object detection and classification of metal polishing shaft surface defects based on convolutional neural network deep learning. *Appl Sci-Basel* 10(1):30
53. Wang YY, Zhang YL, Tan, DP, Zhang YC (2021) Key Technologies and Development Trends in Advanced Intelligent Sawing Equipments. *Chin J Mech Eng* 34:30
54. Zhang HJ, Chen XY, Gong YF, Tian YT, McDonald A, Li H (2020) In-situ SEM observations of ultrasonic cavitation erosion behavior of HVOF-sprayed coatings. *Ultrason Sonochem* 60:104760
55. Ding ZX, Chen W, Wang Q (2011) Resistance of cavitation erosion of multimodal WC-12Co coatings sprayed by HVOF. *Trans Nonferrous Met Soc China* 21(10):2231–2236

**Publisher's note** Springer Nature remains neutral with regard to jurisdictional claims in published maps and institutional affiliations.